ACS OMEGA

http://pubs.acs.org/journal/acsodf

Article

Photocatalytic Decomposition of an Azo Dye Using Transition-Metal-Doped Tungsten and Molybdenum Carbides

Busisiwe Petunia Mabuea, Hendrik Christoffel Swart, and Elizabeth Erasmus*

Cite This: *ACS Omega* 2022, 7, 23401−23411

Read Online

ACCESS | Metrics & More | Article Recommendations | Supporting Information

ABSTRACT: The preparation, characterization, and photocatalytic application of tungsten or molybdenum carbides (Ni-WC, **1**, Co-WC, **2**, Ni-MoC, **3**, Co-MoC, **4**, NiCo-WC, **5**, NiCo-MoC, **6**, NiFe-WC, **7**, and NiFe-MoC, **8**) doped with transition metals (Fe, Co, and Ni) are reported. These transition-metal carbide (TMC) particles show that the submicrometer globular particles agglomerated to form larger particles, with smaller crystallites present on the surface of the large particles. These crystallite sizes range between 4 and 34 nm (as calculated from X-ray diffraction data) depending on the metal dopant and type of carbide. Oxidation of the metal carbides is evident from the two sets of photoelectron lines present in the X-ray photoelectron spectroscopy (XPS) of the W 4f area. The Mo 3d spectra reveal four sets of photoelectron lines associated with oxidized MoO_2 and MoO_3 as well as Mo^{2+} and Mo^{3+} associated with MoC_{1-x}. The XPS of the dopant metals Ni, Co, and Fe also show partial oxidation. The photocatalytic decomposition of Congo red (an azo dye) is used as a model reaction to determine the photocatalytic activities of the transition-metal carbides, which is related to the TMCs' optical band gap energies.

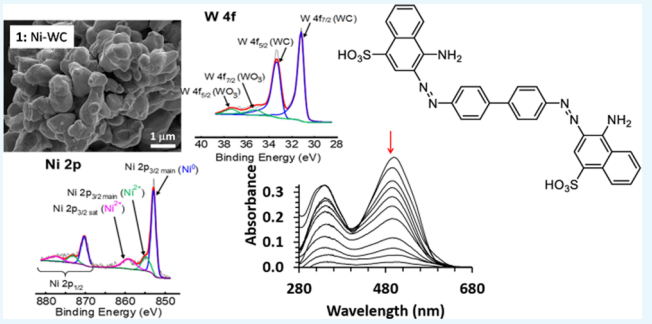

INTRODUCTION

Transition-metal carbides (TMCs), such as molybdenum and tungsten carbides, exhibit remarkably different chemical and physical properties compared to the parent metal or metal oxides (from which they are prepared) on account of the incorporation of the metal−carbon bond. These TMCs have shown potential as a more economical alternative catalyst for an assortment of reactions routinely catalyzed by noble metals. These catalysis reactions include hydrogenation, biomass conversion, water electrolysis, water gas shift reactions, alcohol electrooxidation, and the removal of contaminants (such as nitrogen and sulfur) through hydrotreating.[1] The catalytic properties of TMCs can be enhanced by incorporating a second metal, e.g., Co/MoC and Ni/MoC, due to an improved surface structure.[2] When β-Mo_2C is doped with a small amount of Fe, Co, or Ni, the activity and stability for steam reforming of methanol are improved.[3] It was also reported that the addition of Co to Mo_2C not only improves the activity and selectivity of the Co-doped Mo_2C catalyst toward CO_2 reduction but also improves its durability.[4] Transition metals such as Ni, Co, and Fe are often selected as doping agents because of their ability to combine electrical and optical properties into a single material. They provide a substitute level nearly above the conduction band, which improves the absorption of visible light and utilization, and decrease the electron−hole recombination rate,[2] which is useful during photocatalysis. Recently, metal carbides have also emerged as a promising photocatalyst,[5] Co-doped MoC has been reported to photocatalytically degrade Maxilon Blue GRL 300 basic dye.[2] Since many industries such as textile, plastic, printing, photographic, paper-pulp, paint, and leather factories discard wastes,[6−11] such as hazardous chemicals and synthetic dyes (including highly toxic azo dyes), into rivers and streams, pollution of water has increased dramatically. This then affects the aquatic environment. Water pollution blocks the sunlight from penetrating the water, causing algae to grow and endangering water life. Azo dyes are colored organic compounds having two nitrogen atoms linked to each other (−N═N−). Congo red (see Figure 1 for the chemical structure) is a synthetic dye that belongs to this azo group, with two azo chromophores. It is a highly toxic dye that is very difficult to degrade because of its stable aromatic structure.[12] Congo red is no longer used for dye purposes due to its carcinogenic nature,[13] but it is still used for staining to detect amyloids under a microscope.[14]

There are many methods to treat wastewater, namely, coagulation, electrocoagulation, chlorination, ozonation, flotation, chemical oxidation, filtration, membrane separation, adsorption, and ultrafiltration.[15−23]

Received: March 22, 2022
Accepted: May 27, 2022
Published: June 24, 2022

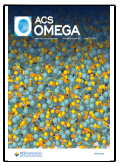

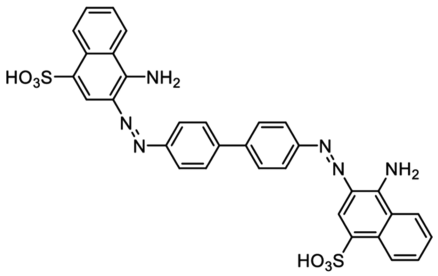

Figure 1. Molecular structure of Congo red.

However, photocatalytic degradation is considered a promising and energy-saving technology to remove high concentrations of biodegradable pollutants. The dye molecule decomposes when it interacts with a photocatalyst in the presence of ultraviolet/visible light from either solar energy or artificial light sources. During the interaction between the dye and the photocatalyst, charge separation is generated by a charge-transfer process. This leads to the formation of reactive oxygen species necessary for the oxidation and subsequent mineralization of the organic contaminants.[24]

Modified TMCs could be a good choice for practical applications in photocatalytic processes because of their efficiency to degrade organic pollutants in wastewater. The present report discusses the synthesis and characterization (X-ray diffraction (XRD), scanning electron microscopy (SEM), time of flight secondary mass spectroscopy (ToF-SIMS), and X-ray photoelectron spectroscopy (XPS)) of tungsten and molybdenum carbides doped with transition metals (Fe, Co, and Ni). These TMC catalysts are tested for the photocatalytic decomposition of the pollutant Congo red, which is an example of an azo dye. Simulated sunlight is used as the irradiation source and the photocatalytic activity of the TMCs is related to the type of carbide, metal dopant, and the particles' optical band gap energy.

EXPERIMENTAL SECTION

Materials. Nickel(II) nitrate hexahydrate [$Ni(NO_3)_2 \cdot 6H_2O$], cobalt(II) nitrate hexahydrate [$Co(NO_3)_2 \cdot 6H_2O$], iron(II) nitrate hexahydrate [$Fe(NO_3)_2 \cdot 6H_2O$], ammonium metatungstate hydrate [$(NH_4)_6H_2W_{12}O_{40} \cdot xH_2O$], ammonium molybdate tetrahydrate [$(NH_4)_6Mo_7O_{24} \cdot 4H_2O$], multiwalled carbon nanotubes, MWCNTs (>98% carbon basis, O.D. × L6−13 nm × 2.5−20 μm), and Congo red (indicator grade) were used in this study. All these analytical grade chemicals were purchased from Merck (Pty) Ltd. and used without further purification.

Synthesis of Transition-Metal Carbide Nanoparticles. A solid-state reaction (carburization method) was used to synthesize transition-metal carbides. The process involves reducing the desired metal precursors using a carbon-based source (MWCNTs) as a reducing agent at high temperatures.

*Synthesis of Ni-WC, **1**.* A combination of $Ni(NO_3)_2 \cdot {}_6H_2O$ (0.049 g; 0.19 mmol; ∼15 equiv), $(NH_4)_6H_2W_{12}O_{40} \cdot xH_2O$ (0.038 g; 0.013 mmol; 1 equiv), and MWCNTs (0.013 g; 0.07 mmol; ∼5 equiv) was mixed homogeneously and ground using a pestle and mortar resulting in a fine powder. The powder was then placed in a furnace for three hours and heated at 950 °C in an H_2-N_2 mixture atmosphere. While the furnace cooled, the gas mixture was replaced by argon until room temperature was attained. This resulted in the isolation of Ni-WC as a gray powder.

*Synthesis of Co-WC, **2**.* Co-WC was prepared by the same procedure used for Ni-WC except $Ni(NO_3)_2 \cdot 6H_2O$ was replaced with 0.049 g (0.17 mmol; ∼13 equiv) cobalt(II) nitrate hexahydrate [$Co(NO_3)_2 \cdot {}_6H_2O$]. This resulted in the isolation of Co-WC as a dark gray powder.

*Synthesis of Ni-MoC, **3**.* Ni-MoC was prepared by the same procedure used for Ni-WC except a combination of $Ni(NO_3)_2 \cdot 6H_2O$ (0.049 g; 0.19 mmol; 10 equiv), $(NH_4)_6Mo_7O_{24} \cdot 4H_2O$ (0.038 g; 0.019 mmol; 1 equiv), and MWCNTs 0.013 g (0.07 mmol; ∼3.7 equiv) was used. This resulted in the isolation of Ni-MoC as a gray powder.

*Synthesis of Co-MoC, **4**.* Co-MoC was prepared by the same procedure used for Ni-WC except a combination of $Co(NO_3)_2 \cdot 6H_2O$ (0.049 g; 0.17 mmol; ∼9 equiv), $(NH_4)_6Mo_7O_{24} \cdot 4H_2O$ (0.038 g; 0.019 mmol; 1 equiv), and MWCNTs 0.013 g (0.07 mmol; ∼3.7 equiv) was used. This resulted in the isolation of Ni-MoC as a gray powder.

*Synthesis of NiCo-WC, **5**.* A combination of $Ni(NO_3)_2 \cdot 6H_2O$ (0.062 g; 0.24 mmol; ∼19 equiv), $Co(NO_3)_2 \cdot 6H_2O$ (0.028 g; 0.096 mmol; ∼7.5 equiv), $(NH_4)_6H_2W_{12}O_{40} \cdot xH_2O$ (0.038 g; 0.013 mmol; 1 equiv), and MWCNTs (0.013 g; 0.07 mmol; ∼5 equiv) was mixed homogeneously with a pestle and mortar. The mixture was transferred to a tube furnace and heated at 950 °C for three hours in an H_2-N_2 mixture atmosphere. While the furnace was cooled, the gas mixture was replaced by argon until room temperature was achieved. This resulted in the isolation of NiCo-WC as a black powder.

*Synthesis of NiCo-MoC, **6**.* NiCo-MoC was prepared by the same procedure used for NiCo-WC except a combination of $Ni(NO_3)_2 \cdot 6H_2O$ (0.062 g; 0.24 mmol; ∼19 equiv), $Co(NO_3)_2 \cdot 6H_2O$ (0.049 g; 0.17 mmol; ∼9 equiv), $(NH_4)_6Mo_7O_{24} \cdot 4H_2O$ (0.038 g; 0.019 mmol; 1 equiv), and MWCNTs (0.013 g; 0.07 mmol; ∼3.7 equiv) was used.

This resulted in the isolation of NiCo-MoC as a light gray powder.

*Synthesis NiFe-WC, **7**.* NiFe-WC was prepared by the same procedure used for NiCo-WC except a combination of $Ni(NO_3)_2 \cdot 6H_2O$ (0.062 g; 0.24 mmol; ∼19 equiv), $Fe(NO_3)_2 \cdot {}_6H_2O$ (0.028 g; 0.07 mmol; ∼5 equiv), $(NH_4)_6H_2W_{12}O_{40} \cdot xH_2O$ (0.038 g; 0.013 mmol; 1 equiv), and MWCNTs (0.013 g; 0.07 mmol; ∼5 equiv) was used.

This resulted in the isolation of NiFe-WC as a black powder.

*Synthesis of NiFe-MoC, **8**.* NiFe-MoC was prepared by the same procedure used for NiCo-WC except a combination of $Ni(NO_3)_2 \cdot 6H_2O$ (0.062 g; 0.24 mmol; ∼19 equiv), $Fe(NO_3)_2 \cdot 6H_2O$ (0.028 g; 0.07 mmol; ∼5 equiv), $(NH_4)_6Mo_7O_{24} \cdot 4H_2O$ (0.038 g; 0.013 mmol; 1 equiv), and MWCNTs (0.013 g; 0.07 mmol; ∼5 equiv) was used.

This resulted in the isolation of NiFe-MoC as a black powder.

Characterization. The crystal structures of various TMCs were analyzed by a PAN analytical X'pert PRO X-ray diffractometer (XRD) using Cu Kα radiation in the range of 25−80°. The average crystallite size (D_{hkl}) was estimated using the Debye−Scherrer equation

$$D_{hkl} = \frac{k\lambda}{\beta . \cos\theta} \quad (1)$$

where k is the crystallite shape coefficient ∼0.9, λ is the wavelength of the radiation, β is the full width at half-maximum (FWHM), and θ is the Braggs angle of diffraction.

Surface particle morphology and elemental composition of TMCs (**1**−**8**) were analyzed using field emission scanning electron microscopy (FE-SEM) coupled with energy-dispersive

https://doi.org/10.1021/acsomega.2c01727
ACS Omega 2022, 7, 23401−23411

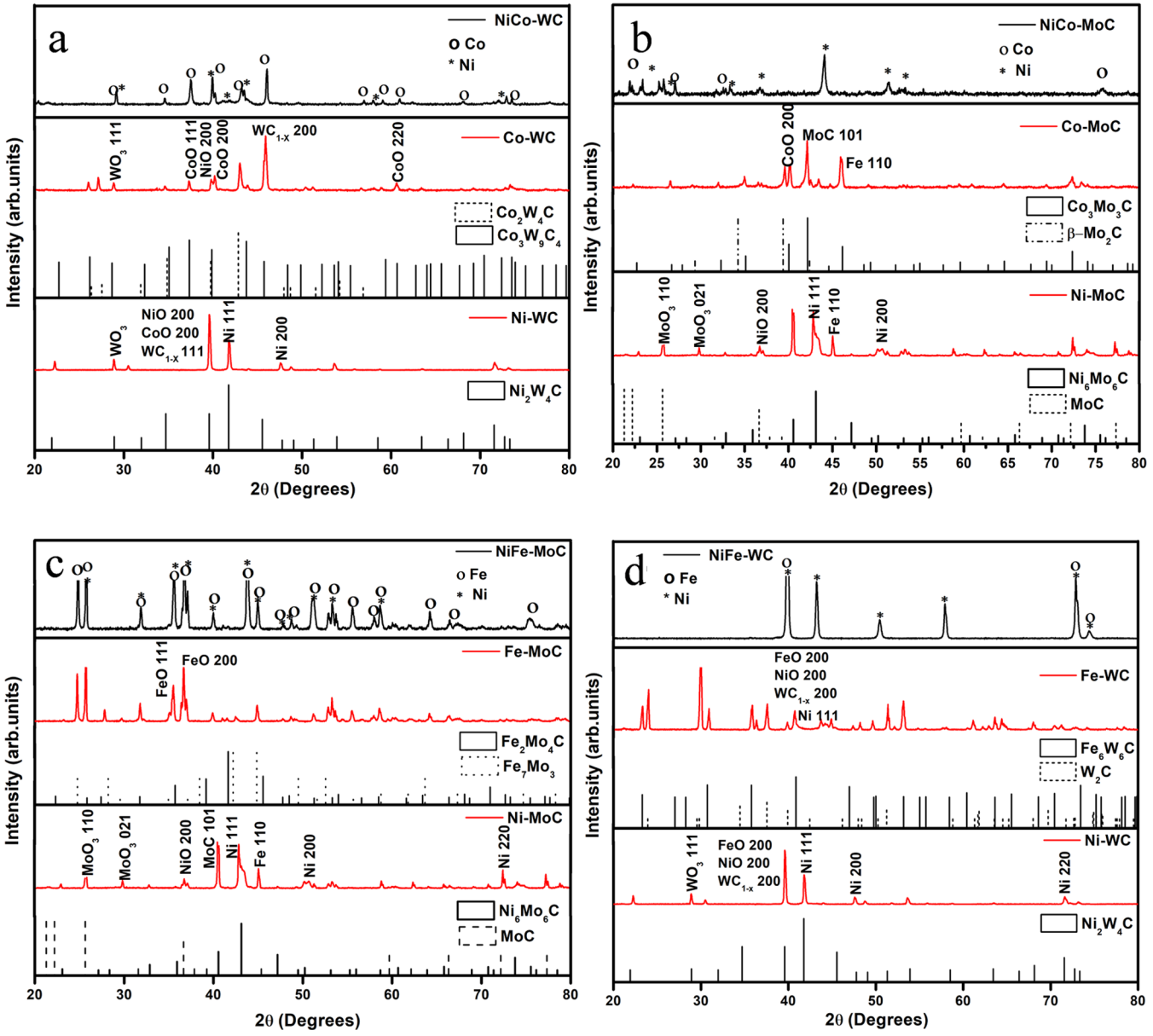

Figure 2. XRD patterns of (a) Co-WC (2), NiCo-WC (5), and Ni-WC (1); (b) Co-MoC (4), NiCo-MoC (6), and Ni-MoC (3); (c) NiFe-WC (7) and Ni-WC (1); and (d) NiFe-MoC (8) and Ni-MoC (3). The XRD peaks in the trimetallic carbides are assigned to the characteristic peaks of both the bimetallic carbides. The peaks marked with an asterisk (*) are not from impurities but from tungsten oxide (WO_3).

X-ray spectroscopy (EDS) respectively. The SEM images were captured using a Shimadzu Superscan ZU SXX-550 electron microscope. The electron beam energies were in the range of 5 keV.

Surface characterization of these TMCs was carried out with a PHI 5000 Versaprobe-Scanning XPS. A monochromatic Al Kα radiation with $h\nu$ = 1486.6 eV was used, which was generated by a 25 W, 15 kV electron beam. A low-energy neutralizer electron gun was used to minimize the charging of the samples. For high-resolution spectra, the hemispherical analyzer pass energy was maintained at 93.90 eV with a 0.1 eV step. The resolution of the PHI 5000 Versaprobe system was FWHM = 0.53 eV at the pass energy of 23.5 eV and FWHM = 1.44 eV at the pass energy of 93.9 eV. The X-ray beam size used for the XPS measurements was 10 μm. The pressure during acquisition was less than 1×10^{-8} Torr. All of the absolute binding energies of the photoelectron spectra were corrected with a C 1 s signal at 284.8 eV (the lowest binding energy of the simulated adventitious C 1 s photoelectron line).[30] The XPS data was analyzed by a Multipak version 8.2c computer software,[31] and applying Gaussian−Lorentz fits (the Gaussian/Lorentz ratios were always >95%). The neat samples were held in place on the sample holder by means of carbon tape, and the samples were sputtered with different Ar^+ ion beam energies in the range of 0.5−4.0 keV.

ToF-SIMS is a surface characterization technique used to investigate the composition of a sample. This is achieved by sputtering the surface with an ion beam and analyzing the collected secondary ions. ToF-SIMS measurements were conducted on a PHI TRIFT V nanoTOF. The UV−vis absorption spectra of the TMCs, for determining their band gap energy, were recorded using a Perkin Elmer Lambda 950 UV−vis at room temperature in the range of 300−800 nm.

https://doi.org/10.1021/acsomega.2c01727
ACS Omega 2022, 7, 23401−23411

The optical band gap energy is an important parameter of photocatalytic performance. The optical band gap energies of the transition-metal carbides were calculated from the % reflectance *vs* wavelength graphs using Tauc's equation (eq 2)

$$(\alpha h\nu) = A(h\nu - E_g)^n \quad (2)$$

where α is an absorption coefficient, $h\nu$ is the photon's energy, A is the proportional constant, E_g is the band gap energy, and n is the nature of the sample transition. The value of n for allowed direct, allowed indirect, forbidden direct, and forbidden indirect transitions are 0.5, 2, 3/2, and 3, respectively.[25] According to Kubelka−Munk,[26] α is proportional to the measured reflectance (R) and can be expressed by

$$(\alpha) \propto F(R) = \frac{(1 - 2R)^2}{2R} \quad (3)$$

This then allows the construction of a Tauc plot, which shows a relationship between the absorption coefficient and the optical band gap. The optical band gap of the TMCs was determined by extrapolating the linear portion of the curves (see the Supporting Information for the graphs).

Photocatalytic Application (Congo Red Dye Degradation). The photocatalytic activity of the transition-metal-doped TMC particles was studied for the photocatalytic degradation of Congo red dye (Figure 1) under simulated sunlight irradiation using a 350 W metal halide lamp in the open air at room temperature. Fifty milligrams of the catalyst was placed in a 250 cm^3 beaker containing 100 cm^3 of dye solution (20 mg dm^{-3}, pH = 7.0), which were stirred magnetically. Five cubic centimeter samples were taken at random time intervals and the change in absorption of the Congo red was measured using a Shimadzu CPS-240A UV−vis spectrophotometer, corresponding to λ_{max} of dye = 495 nm. Dark adsorption (in the presence of a catalyst but no light) and photolysis (exposure to light but no catalyst) degradation reactions were carried out to differentiate between the adsorption and photocatalytic degradation. Adsorption experiments were performed in the dark, while photocatalytic tests were performed with light irradiation.

RESULTS AND DISCUSSION

Synthesis. Various transition-metal-doped tungsten and molybdenum carbides (Ni-WC, **1**, Co-WC, **2**, Ni-MoC, **3**, Co-MoC, **4**, NiCo-WC, **5**, NiCo-MoC, **6**, NiFe-WC, **7**, and NiFe-MoC, **8**) were prepared by carbothermal reduction. This process involves the reduction of the desired combination of metal oxides at a high temperature (950 °C) using MWCNTs as the reducing agent in an H_2−N_2 atmosphere.

Structural Analysis. The crystal phase, purity, and crystallite size of the TMCs, **1**−**8**, were analyzed by XRD and are displayed in Figure 2. Acceptable matches were observed for the bimetallic catalysts. The Co-WC (**1**) pattern correlated to the $Co_3W_9C_4$ (ICDD 01−072−1362) and Co_6W_6C (ICDD 00-023-0939), the Ni-WC (**2**) pattern to the Ni_2W_4C (ICDD 00-020-0796), and Ni-MoC to Ni_6Mo_6C (ICDD no. 03-065-4436) and MoC (ICDD no. 20-0748), while Co-MoC corresponded to Co_3Mo_3C (ICDD no. 03-065-7128) and β-Mo_2C (ICDD no. 45−1014), the Fe-WC to Fe_6W_6C (ICDD no. 01−089−2616) and W_2C (ICDD no. 01-089-2371), and Fe-MoC to Fe_2Mo_4C (ICDD no. 01-089-4884) and Fe_7Mo_3 (ICDD no. 00-045-1230). The trimetallic carbides (NiCo-WC, **5**, NiCo-MoC, **6**, NiFe-WC, **7**, and NiFe-MoC, **8**) matched well with their corresponding bimetallic carbides.

From the crystallite sizes of **1**−**8** presented in Table 1, the Co-doped TMCs displayed smaller crystallite sizes for the bimetallic

Table 1. Average Crystallite Sizes Calculated for 1−8 from the XRD Data Using (eq 1)[a]

no.	sample	average crystallite size (nm)	% decolorization of Congo red after 25 min	optical band gap energy (eV)
1	Ni-WC	34	86	2.77
2	Co-WC	4	66	2.50
3	Ni-MoC	25	94	2.00
4	Co-MoC	22	72	1.83
5	NiCo-WC	7	97	2.3
6	NiCo-MoC	15	72	2.34
7	NiFe-WC	22	44	1.97
8	NiFe-MoC	32	41	1.66

[a]The % decolorization of Congo red after 25 min of photocatalytic reaction time in the presence of the TMC catalyst. The optical band gap energy was determined using the Tauc plots of **1**−**8**.

TMCs (**2** and **4** *vs* **1** and **3**) and trimetallic TMCs (**5** and **7** *vs* **6** and **8**), while the WC trimetallic TMCs (**5** and **6** *vs* **7** and **8**) displayed smaller crystallites compared to MoC.

Morphology and Chemical Composition Analysis. Figure 3 shows the SEM images with a low magnification of **1**−**8** (the high-magnification SEM and EDS data are presented in the Supporting Information). Apart from **8**, the TMCs (**1**−**7**) show agglomeration of submicrometer globular particles into larger particles. Small crystallites can be observed on the surface of the large particles in the high-magnification SEM images. This type of morphology is consistent with other transition-metal-doped tungsten and molybdenum carbides reported by Regmi et al.[27] EDS confirms the presence of the desired elements in the TMCs **1**−**8** (see the Supporting Information for the EDS data).

Surface Composition and Chemical State Analysis (XPS). XPS is a convenient technique for identifying the elements present in a sample, the oxidation state of the elements, and even the chemical environment that surrounds the element.

The measured binding energies for the main photoelectron lines were charged correctly against the simulated adventitious carbon set at 284.8 eV.[28] Simulated curve fitting of the C 1s area of the TMCs (**1**, **2**, and **5**−**8**) enabled the location of the carbide photoelectron line at *ca.* 283.5 eV (see Table 2 and Figure 4), which correlates well with the reported binding energy range of 283.3−283.5 eV for WC_{1-x}.[29−31]

Figure 4 compiles as representative examples the C 1s, W 4f, Ni 2p, and Fe 2p high-resolution spectra of **7** as well as the Co 2p area of **2** and the Mo 3d area of **8** (the XPS of all of the metals of **1**, **2**, and **5**−**8** are presented in the Supporting Information), while the data extracted from the XPS are reported in Tables 2 and 3.

Two sets of photoelectron lines were observed for the W 4f spectra of all of the W-containing TMCs (**1**, **5**, and **7**). The $4f_{7/2}$-$4f_{5/2}$ doublets displayed a spin−orbit splitting $\Delta BE \approx 2.2$ eV. The photoelectron lines at *ca.* 31.5 and 35.2 eV were assigned to the W $4f_{7/2}$ line of WC and WO_3, respectively. These binding energy assigned to the WC photoelectron lines were in accordance with the range values of 31.5−31.8 eV reported

https://doi.org/10.1021/acsomega.2c01727
ACS Omega 2022, 7, 23401−23411

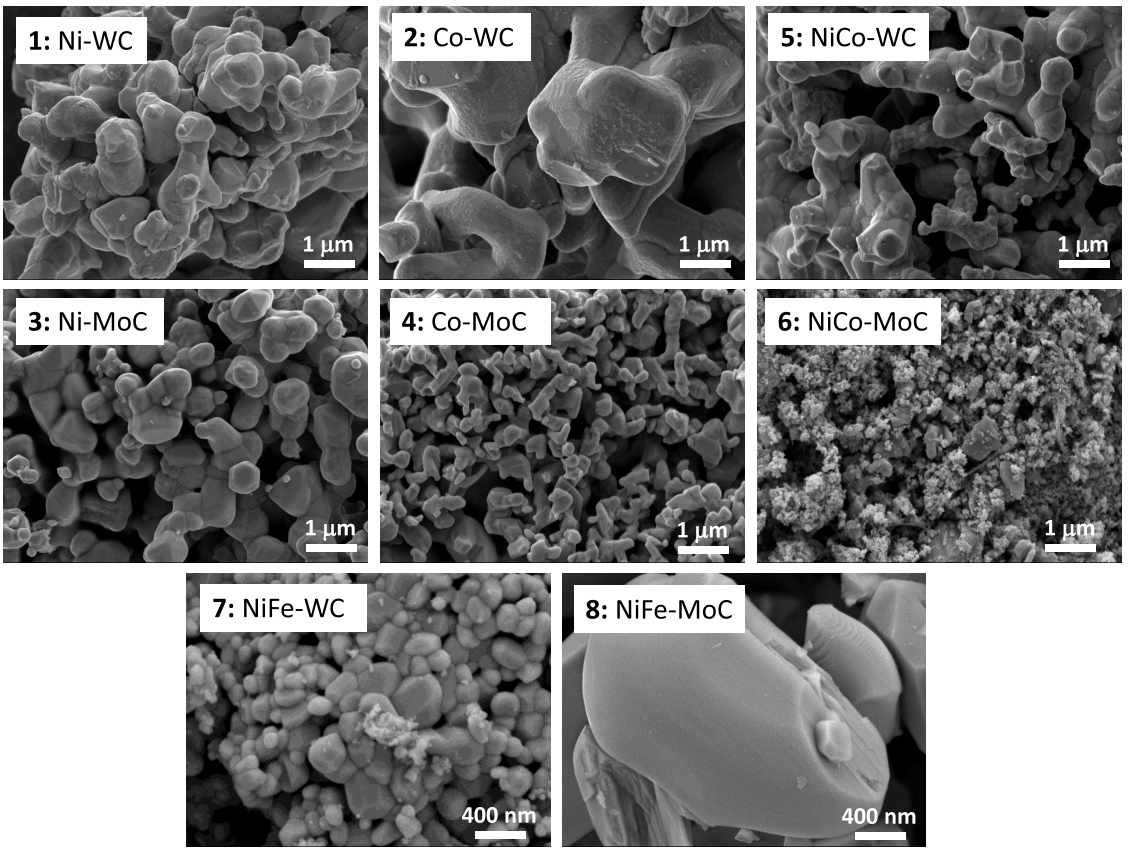

Figure 3. SEM images of **1**−**8**.

for the WC_{1-x} phase in the literature.[29−31] Partial surface oxidation was revealed by the presence of a $4f_{7/2}$-$4f_{5/2}$ doublet between 35 and 38 eV corresponding to WO_3.[32]

Molybdenum is present in a mixed-valence state for the MoC TMCs (**6** and **8**). Four different valence states, namely, 2+, 3+, 4+, and 6+, were detected in the XPS Mo 3d spectra (see Figure 4 and Table 2). The binding energy of the Mo $2d_{5/2}$ photoelectron lines of the higher-valence states Mo^{4+} and Mo^{6+} present at 231.4 and 232.6 eV (with a *ca.* $\Delta BE \approx 3.1$ eV), respectively, were assigned to the partial oxidation (MoO_2 and MoO_3) of the MoC_{1-x} surface.[33−35] The lower valence states Mo^{2+} and Mo^{3+}, which are associated with the carbide, revealed Mo $2d_{5/2}$ photoelectron lines at *ca.* 228.7 and 230.0 eV, respectively, in correlation with that reported for MoC_{1-x} in the literature.[33,34,36,37]

Ni is present in two different valence states (0 and 2+) in **1** and **5**−**8**, as evident from its Ni 2p XPS (see Figure 4 and Table 2). The Ni $2p_{3/2}$ simulated photoelectron lines at *ca.* 852.9 eV are characteristic of metallic Ni^0. The lines at *ca.* 855.2 eV and its associated satellite structures situated at 859.6 eV are assigned to Ni^{2+}, indicating that Ni was partly oxidized.[38] The degree of oxidation of Ni was found to be *ca.* 7% higher when doped in Mo than when doped in W (**6** and **8** *vs* **5** and **7**). Also, when the codopant was Co (**5** and **6**), a higher degree of oxidation occurred for Ni as compared to when Fe was used as a codopant (**7** and **8**).

The Co 2p envelope (of **2**, **5**, and **6**) was deconvoluted to fit three sets of Co $2p_{3/2}$−Co $2p_{1/2}$ doublets. The two simulated photoelectron lines at *ca.* 778.7 and 793.7 eV corresponded to Co $2p_{3/2}$ and Co $2p_{1/2}$, respectively, of metallic Co^0. The Co $2p_{3/2}$ photoelectron line positions at *ca.* 781.0 and 786.3 eV were assigned to the main and satellite structure, respectively, of Co^{2+} and/or Co^{3+} associated with oxidized cobalt.[39]

Mixed valencies were also observed for the iron in **7** and **8**. According to the simulated fitting of the photoelectron lines, *ca.* 35% of the iron was present as metallic Fe^0. These Fe^0 lines presented as sharp well-defined peaks at *ca.* 707 eV with a full width at half-maximum (FWHM) of *ca.* 1.2 eV. Further deconvolution of the Fe 2p envelope indicated the main photoelectron line (*ca.* 709.3 eV) and satellite structures (712.5 eV) for Fe^{2+}, which is associated with FeO.[40]

Although not normally used as a quantitative technique, XPS accurately detected the ratios between atomic %,[41−48] thus giving a good indication (estimation) of the composition. A summary of the atomic ratios between the metals as well as the ratios between different compounds (e.g., WC and WO) is given in Table 3. Using these atomic ratios obtained between the metals, as well as the relative % of metal species (as defined by their oxidation state and binding energy position) from the XPS, it is possible to estimate the stoichiometric compositions of **1**−**8**:

1: $Ni_{0.8}(NiO)_{0.6}(WC)_{0.8}(WO_3)_{0.2}$
2: $Co_{0.6}(CoO)_{0.8}W_{0.1}(WC)_{0.5}(WO_3)_{0.4}$
5: $Ni_{0.6}(NiO)_{0.5}\ Co_{0.5}(CoO)_{1.2}(WC)_{0.6}(WO_2)_{0.4}$
6: $Ni_{0.5}(NiO)_{0.5}\ Co_{0.4}(CoO)_{1.2}(MoC_{1-x})_{0.4}(MoO_{2/3})_{0.6}$
7: $Ni_{0.7}(NiO)_{0.4}Fe_{0.4}(FeO)_{0.5}(WC)_{0.9}(WO_2)_{0.1}$
8: $Ni_{0.4}(NiO)_{0.2}Fe_{0.2}(FeO)_{0.9}(MoC_{1-x})_{0.7}(MoO_{2/3})_{0.3}$

Time-of-Flight Secondary Ion Mass Spectrometry Analysis. The mass spectra of both the positive and negative secondary ions were recorded for the trimetallic carbides **5**−**8**.

The false color overlay ToF-SIMS images (both positive and negative modes) of the different elements of the trimetallic

https://doi.org/10.1021/acsomega.2c01727
ACS Omega 2022, 7, 23401−23411

Table 2. Binding Energies (BE Measured in eV) of the Main Photoelectron Lines and If Applicable the Satellite Structures of the W $4f_{7/2}$, Mo $3d_{5/2}$, C 1s, O 1s, Ni $2p_{3/2}$, Co $2p_{3/2}$, and Fe $2p_{3/2}$ of 1, 2, and 5−8

	W $4f_{7/2}$		Mo $3d_{5/2}$				C 1s	O 1s	Ni $2p_{3/2}$			Co $2p_{3/2}$			Fe $2p_{3/2}$		
	WC	$WO_{2/3}$	Mo^{2+}	Mo^{3+}	Mo^{4+}	Mo^{6+}	carbide	oxide	Ni^0	Ni^{2+}	Ni_{sat}	Co^0	$Co^{2+/3+}$	Co_{sat}	Fe^0	Fe^{2+}	Fe_{sat}
1: Ni-WC	31.4	35.6					283.8	530.8	852.4	855.4	860.2						
2: Co-WC	31.6	35.5					283.8	530.9				778.7	780.9	786.3			
5: NiCo-WC	31.5	33.6					283.7	529.9	853.2	855.7	860.5	778.6	780.8	786.3			
6: NiCo-MoC			228.5	229.7	231.1	232.8	283.6	530.9	853.4	855.2	859.1	778.8	781.4	786.3			
7: NiFe-WC	31.6	35.9					283.1	530.7	852.9	854.8	859.0				706.9	709.0	712.2
8: NiFe-MoC			229.0	230.3	231.6	232.5	283.5	530.9	852.9	855.1	859.0				707.1	709.5	712.8

carbides **5**−**8** are shown in Figure 5. The emitted secondary ions captured by the detector are within the area of 100 × 100 μm^2. An image with high intensity means high ionic concentration, while a low color intensity means low ionic concentration. From the ToF-SIMS images in Figure 5, the ions of the dopants are uniformly distributed in the metal carbide particles, indicating a homogeneous scattering of all of the different transition metals, with no agglomeration.

Photocatalytic Decomposition of Congo Red. The photocatalytic activity of TMCs (**1**−**8**) was compared using the model decomposition of the Congo red under simulated sunlight irradiation. Congo red is a toxic azo dye that is very difficult to decompose because of its stable aromatic structure.[12]

For a comparison of the removal efficiency of various TMCs (**1**−**8**), Congo red dye decomposition was executed in the dark (dark absorption, catalyst but no light), photolysis (no catalyst but in light), and photocatalytic conditions (in the presence of both catalyst and light). The photocatalytic decomposition process was performed under the same conditions for all of the TMCs: initial Congo red concentration = 20 mg dm^{-3}, catalyst loading = 50 mg, solution pH = 7.0, irradiation = 350 W metal halide lamp, and λ_{max} of Congo red = 495 nm.

Figure 6 shows the UV−vis absorption spectra of the Congo red solution over time during photolysis (in the presence of light and no catalyst) and (b) dark absorption (in the presence of a catalyst but in the absence of light) and photocatalytic decomposition (in the presence of light and a catalyst). Ni-WC (1) is presented as a representative example (graphs of 2−8 are presented in the Supporting Information). Negligible degradation was observed in both the dark absorption and photolysis, as can be seen from the lack of decrease in the peak intensity in Figure 6a,b, indicating that both light and photocatalyst are needed for the effective decomposition of dye molecules in solution. The decomposition of the dye's molecules in Figure 6c is confirmed by the decrease in the intensity of the bands in relation to time. The absorption peaks gradually decrease without a change in the wavelength of λ_{max} before disappearing. This is in agreement with a report by Dantas et al., who analyzed the photocatalytic degradation of the Maxilon Blue GRL 300 textile dye in the presence of the Ni-Mo_2C catalyst at different time intervals. The absorbance results show a decrease in the peak intensity over time, implying a degradation of dye molecules in solution.[2]

The photocatalytic decolorization is calculated from the dye's concentration (C/C_0) over time (see Figure 6d and graphs in the Supporting Information). C_0 is the initial concentration of the dye solution and C is the concentration at time t (min).

The photocatalytic decolorization fraction (C/C_0) of the TMCs decrease drastically compared to dark absorption and photolysis, affirming that visible light irradiation and a photocatalyst in this case TMCs are needed for the decomposition of Congo red.

To compare the activity of the photocatalytic properties of **1**−**8**, the % decolorization of Congo red was determined after 25 min reaction time (see Table 1 and Figure 7). NiCo-WC (97.1%) displayed the highest decolorization % after 25 min, closely followed by Ni-MoC, with 94% decolorization after 25 min. This was much better when compared to the that of reported for Mo_2C by Dantas et al., who showed the maximum decolorization of 90.5% for Congo red after 1 h. From the data in Figure 7, it could be concluded that the Ni-doped carbide derivatives (NiCo-WC, Ni-MoC, and Ni-WC) were the most

https://doi.org/10.1021/acsomega.2c01727
ACS Omega 2022, 7, 23401−23411

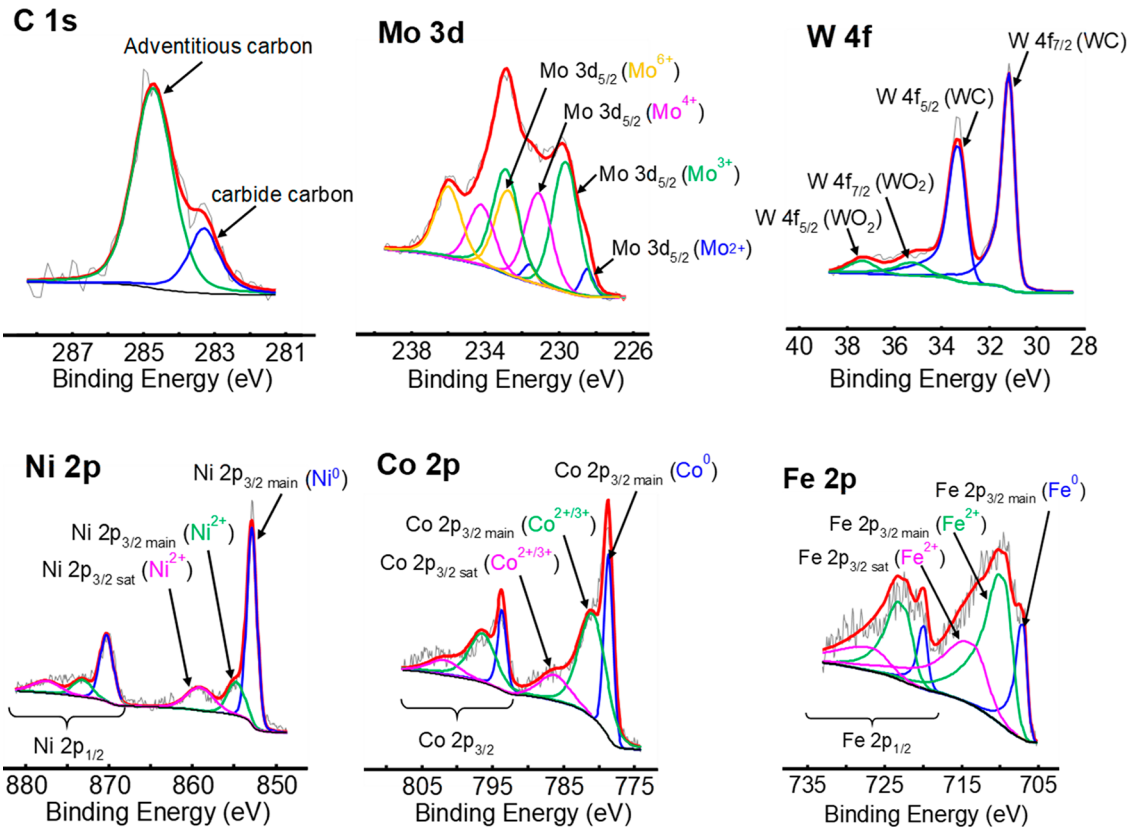

Figure 4. High-resolution XPS scans of the C 1s (of 7), Mo 3d (of 8), W 4f (of 7), Ni 2p (of 7), Co 2p (of 2), and Fe 2p (of 8) areas showing the simulated components. The red line indicates the accumulative simulation of all of the fitted components.

Table 3. Atomic Ratios (as Estimated from the XPS Data) between Different Metals of the Prepared TMCs 1−8

	W				Ni			Co			Fe			Mo		
	W_{tot}	W^0	WC	WO	Ni_{tot}	Ni^0	NiO	Co_{tot}	Co^0	CoO	Fe_{tot}	Fe^0	FeO	Mo_{tot}	MoC	MoO
1: Ni-WC	1.0		0.82	0.18	1.39	0.80	0.59									
2: Co-WC	1.0	0.10	0.53	0.37				1.36	0.77	0.59						
5: NiCo-WC	1.0		0.57	0.43	1.11	0.59	0.51	1.74	1.24	0.50						
6: NiCo-MoC					1.04	0.53	0.51	1.60	1.19	0.41				1.0	0.41	0.59
7: NiFe-WC	1.0		0.88	0.12	1.05	0.69	0.36				0.86	0.49	0.37			
8: NiFe-MoC					0.60	0.40	0.20				1.04	0.87	0.16	1.0	0.70	0.30

active photocatalysts. While the Co- and Fe-doped carbides result in the least decolorization after 25 min.

It is also reported that when Mo_2C is doped with Co the % decolorization decreased from 86.7% for neat Mo_2C to 83.7% for the 10% Co-doped Mo_2C at a pH of 9. This affirms our results that doping with Co results in a decrease in photocatalytic activity.

A rough general trend favors an increase in band gap energy (Table 1), which is associated with an increase in the decolorization activity. For materials having large band energies, the recombination rate of the electron−hole pair is reduced, causing the pair to have a longer time to interact with surface molecules, in turn resulting in better photocatalytic activity (faster decolorization).[49,50]

The graph comparing the optical band gap energy of the TMCs against the % decolorization of Congo red after 25 min of photocatalytic reaction in the presence of the TMCs is shown in Figure 7. The data points on this graph were grouped into three sets: TMCs containing WC (1, 2, and 7), TMCs containing MoC (3, 4, and 8), and TMCs doped with both Ni and Co (5 and 6). For the WC (1: BGE = 2.77, 86% decolorization; 2: BGE = 2.5, 66% decolorization; and 7: BGE = 1.97, 44% decolorization) and MoC (3: BGE = 2.00, 94% decolorization; 4: BGE = 1.83, 72% decolorization; and 8: BGE = 1.66, 41% decolorization) containing TMCs, the % decolorization of the Congo red increases as the band gap energy increases during the photocatalytic reaction and correspondingly the photocatalytic activity of the TMC. This increase in the photocatalytic activity associated with an increase in the band gap energy is more pronounced for the WC-containing TMCs than for the MoC containing TMCs (as can be seen by the slope of the graphs). For the NiCo-containing TMCs (5: BGE = 2.3, 97% decolorization; and 6: BGE = 2.34, 72% decolorization), change in band gap energy seems to have a negligible influence on the photocatalytic activity of the TMCs.

No relationship could be established between the amount of oxidation of the carbides or the doping metal or the amount of doping metals added.

https://doi.org/10.1021/acsomega.2c01727
ACS Omega 2022, 7, 23401−23411

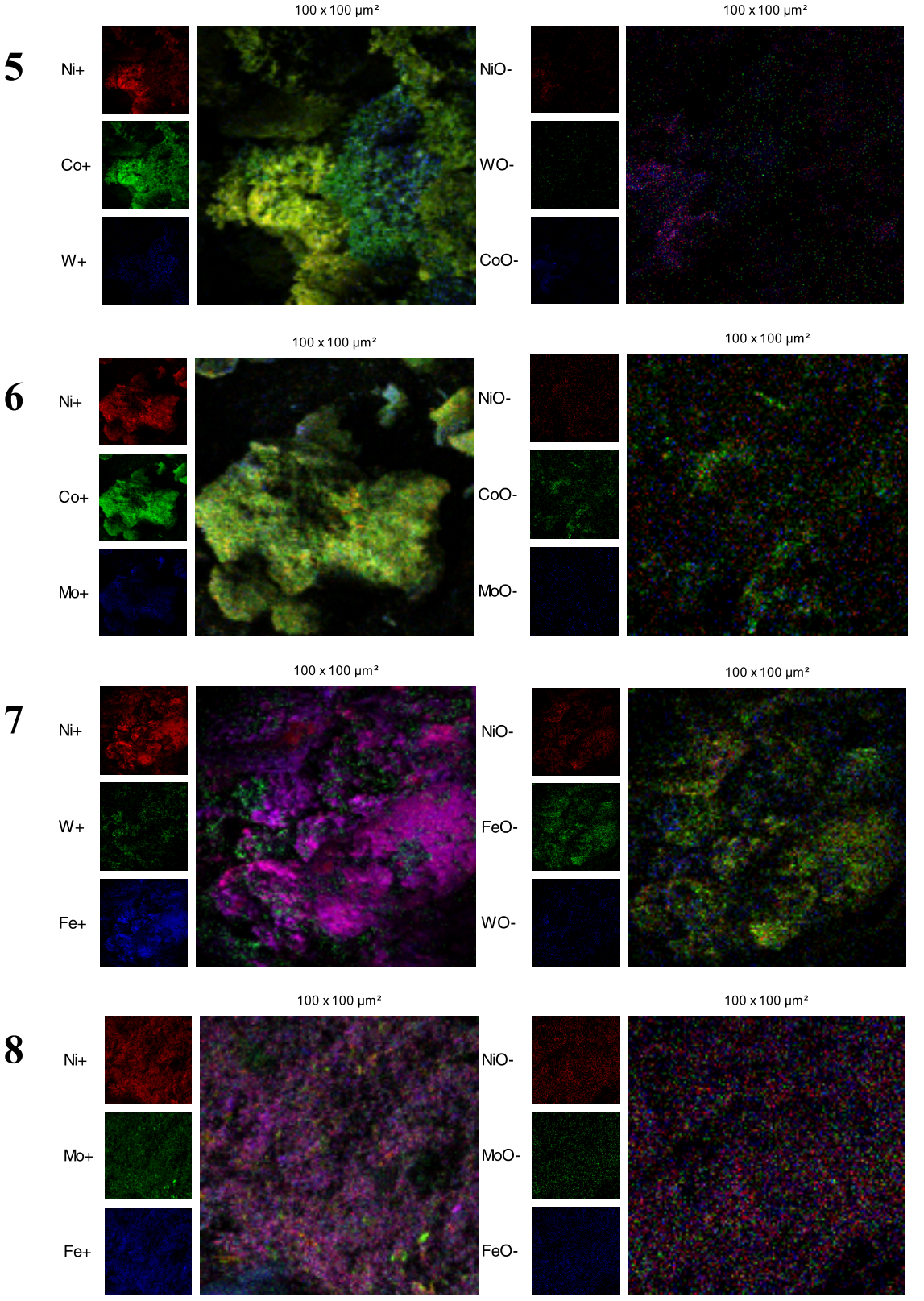

Figure 5. ToF-SIMS images collected from (left column) the positive-ion mode and (right column) the negative-ion mode of 5−8.

CONCLUSIONS

Various transition-metal carbides (Ni-WC, **1**, Co-WC, **2**, Ni-MoC, **3**, Co-MoC, **4**, NiCo-WC, **5**, NiCo-MoC, **6**, NiFe-WC, **7**, and NiFe-MoC, **8**) were prepared by the carbothermal reduction of the parent metal oxides. It was found that the crystallite sizes were dependent on the dopant and metal carbide. The Co-doped TMCs displayed smaller crystallite sizes for the bimetallic TMCs (**2** and **4** *vs* **1** and **3**) and trimetallic TMCs (**5** and **7** *vs* **6** and **8**), while the WC trimetallic TMCs (**5** and **6** *vs* **7** and **8**) displayed smaller crystallites compared to

https://doi.org/10.1021/acsomega.2c01727
ACS Omega 2022, 7, 23401−23411

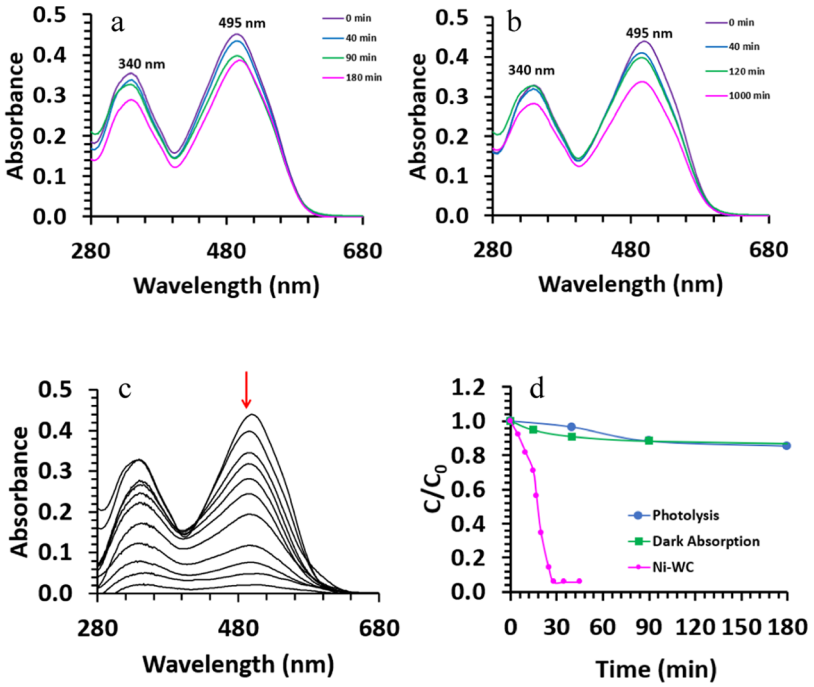

Figure 6. UV−vis absorption spectra of the Congo red solution during (a) photolysis, (b) dark absorption (with Ni/WC, 1), and (c) photocatalytic decomposition (time 0−45 min) with Ni-WC as an example (graphs of 2−8 are presented in the Supporting Information). (c) Photocatalytic decolorization graph (of 1) showing concentration (C/C_0) *vs* time measured at λ = 495 nm. (d) The kinetics of photocatalytic degradation of Congo red under different conditions: in the dark with catalyst (green square), without catalyst under irradiation (blue dot), and with catalyst under irradiation (magenta dot).

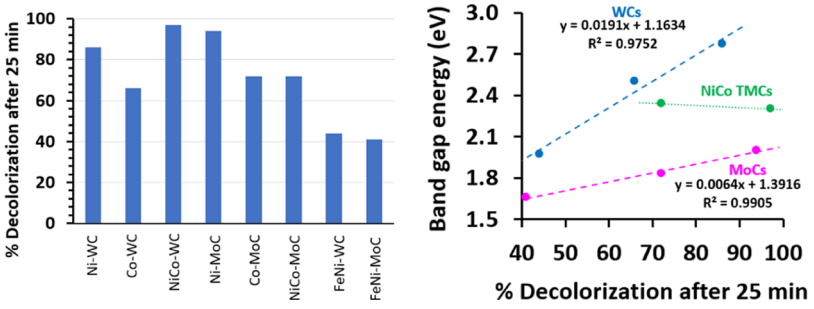

Figure 7. Left: % Decolorization after 25 min of photocatalytic reaction time. Right: Comparison between the optical band gap energy of the TMCs and the % decolorization of Congo Red after 25 min photocatalytic reaction in the presence of TMCs.

MoC. From the SEM images, the TMCs (**1**−**7**) showed agglomeration of submicrometer globular particles into larger particles, the 4−34 nm crystallites (as determined by XRD) can be observed on the surface of the large particles.

Partial oxidation of all of the metals in the TMCs **1**−**8** occurred as was evident from the XPS, which showed the presence of the metal oxides along with the carbide and metallic photoelectron lines. Additionally, it was found that the ions detected by ToF-SIMS were not distributed evenly. Despite the oxidation that occurred and the uneven distribution of the ion in the TMCs, good photocatalytic activity was obtained for the decomposition of Congo red. This photocatalytic activity is highly dependent on the type of carbide, metal dopant, and the band gap energy of the material. WC-containing TMCs with higher band gap energies (Ni-WC, **1**, band gap energy = 2.77 eV; NiCo-WC, **5**, band gap energy = 2.30 eV) gave the best overall decolorization after 25 min (Ni-WC, **1**, % decolorization after 25 min = 86%; NiCo-WC, **5**, % decolorization after 25 min = 97%) and accordingly the best photocatalytic activity. However, Ni-MoC, **3**, displayed a high band gap energy of 2.00 eV and resulted in very good photocatalytic activity with 94% decolorization after 25 min. The Fe-doped carbides NiFe-WC, **7**, and NiFe-MoC, **8**, displayed a poor photocatalytic activity of 44 and a decolorization of 41% after 25 min.

■ ASSOCIATED CONTENT

Supporting Information

The Supporting Information is available free of charge at https://pubs.acs.org/doi/10.1021/acsomega.2c01727.

Additional SEM images, EDS data, XPS spectra, and time-based UV−vis spectra of the photocatalytic decomposition of Congo red. Decolorization graphs and the Tauc plots used to determine the TMCs band gap energies (PDF)

https://doi.org/10.1021/acsomega.2c01727
ACS Omega 2022, 7, 23401−23411

AUTHOR INFORMATION

Corresponding Author

Elizabeth Erasmus − *Department of Chemistry, University of the Free State, Bloemfontein 9300, South Africa;* orcid.org/0000-0003-0546-697X; Email: erasmuse@ufs.ac.za

Authors

Busisiwe Petunia Mabuea − *Department of Physics, University of the Free State, Bloemfontein 9300, South Africa*

Hendrik Christoffel Swart − *Department of Physics, University of the Free State, Bloemfontein 9300, South Africa;* orcid.org/0000-0001-5233-0130

Complete contact information is available at: https://pubs.acs.org/10.1021/acsomega.2c01727

Notes

The authors declare no competing financial interest.

ACKNOWLEDGMENTS

The Department of Science and Technology of South Africa (Grand 84415) is acknowledged for financial support (HCS). The Central Research Fund of the University of the Free State, Bloemfontein, South Africa is also acknowledged for financial support.

REFERENCES

(1) dos Santos Politi, J. R.; Viñes, F.; Rodriguez, J. A.; Illas, F. Atomic and Electronic Structure of Molybdenum Carbide Phases: Bulk and Low Miller-Index Surfaces. *Phys. Chem. Chem. Phys.* **2013**, *15*, 12617.

(2) Dantas, S. L. A.; Silva, M. M. S.; Gomes, Y. F.; Lopes-Moriyama, A. L.; Souza, C. P.; Corrêa, M. A. Photocatalytic Degradation Tests with Cobalt-Doped Molybdenum Carbides. *Appl. Phys. A: Mater. Sci. Process.* **2021**, *127*, 120.

(3) Ma, Y.; Guan, G.; Shi, C.; Zhu, A.; Hao, X.; Wang, Z.; Kusakabe, K.; Abudula, A. Low-Temperature Steam Reforming of Methanol to Produce Hydrogen over Various Metal-Doped Molybdenum Carbide Catalysts. *Int. J. Hydrogen Energy* **2014**, *39*, 258−266.

(4) Porosoff, M. D.; Yang, X.; Boscoboinik, J. A.; Chen, J. G. Molybdenum Carbide as Alternative Catalysts to Precious Metals for Highly Selective Reduction of CO 2 to CO. *Angew. Chem., Int. Ed.* **2014**, *53*, 6705−6709.

(5) Powar, N. S.; Hiragond, C. B.; Bae, D.; In, S.-I. Two-Dimensional Metal Carbides for Electro- and Photocatalytic CO2 Reduction: Review. *J. CO2 Util.* **2022**, *55*, No. 101814.

(6) Immich, A. P. S.; Ulson de Souza, A. A.; Ulson de Souza, S. M. deA. G. Removal of Remazol Blue RR Dye from Aqueous Solutions with Neem Leaves and Evaluation of Their Acute Toxicity with Daphnia Magna. *J. Hazard. Mater.* **2009**, *164*, 1580−1585.

(7) Afkhami, A.; Moosavi, R. Adsorptive Removal of Congo Red, a Carcinogenic Textile Dye, from Aqueous Solutions by Maghemite Nanoparticles. *J. Hazard. Mater.* **2010**, *174*, 398−403.

(8) Zhao, X.; Wang, W.; Zhang, Y.; Wu, S.; Li, F.; Liu, J. P. Synthesis and Characterization of Gadolinium Doped Cobalt Ferrite Nanoparticles with Enhanced Adsorption Capability for Congo Red. *Chem. Eng. J.* **2014**, *250*, 164−174.

(9) Lu, L.; Li, J.; Ng, D. H. L.; Yang, P.; Song, P.; Zuo, M. Synthesis of Novel Hierarchically Porous Fe3O4@MgAl−LDH Magnetic Microspheres and Its Superb Adsorption Properties of Dye from Water. *J. Ind. Eng. Chem.* **2017**, *46*, 315−323.

(10) Liu, D.; Lei, W.; Qin, S.; Chen, Y. Template-Free Synthesis of Functional 3D BN Architecture for Removal of Dyes from Water. *Sci. Rep.* **2015**, *4*, No. 4453.

(11) Sinha, A. K.; Pradhan, M.; Sarkar, S.; Pal, T. Large-Scale Solid-State Synthesis of Sn−SnO 2 Nanoparticles from Layered SnO by Sunlight: A Material for Dye Degradation in Water by Photocatalytic Reaction. *Environ. Sci. Technol.* **2013**, *47*, 2339−2345.

(12) Koe, W. S.; Lee, J. W.; Chong, W. C.; Pang, Y. L.; Sim, L. C. An Overview of Photocatalytic Degradation: Photocatalysts, Mechanisms, and Development of Photocatalytic Membrane. *Environ. Sci. Pollut. Res.* **2020**, *27*, 2522−2565.

(13) Hunger, K.; Mischke, P.; Rieper, W.; Raue, R.; Kunde, K.; Engel, A. Azo Dyes. In *Ullmann's Encyclopedia of Industrial Chemistry*; Wiley-VCH Verlag GmbH & Co. KGaA: Weinheim, Germany, 2000.

(14) Yakupova, E. I.; Bobyleva, L. G.; Vikhlyantsev, I. M.; Bobylev, A. G. Congo Red and Amyloids: History and Relationship *Biosci. Rep.* 2019, 391 DOI: 10.1042/BSR20181415.

(15) Teh, C. Y.; Budiman, P. M.; Shak, K. P. Y.; Wu, T. Y. Recent Advancement of Coagulation−Flocculation and Its Application in Wastewater Treatment. *Ind. Eng. Chem. Res.* **2016**, *55*, 4363−4389.

(16) Tahreen, A.; Jami, M. S.; Ali, F. Role of Electrocoagulation in Wastewater Treatment: A Developmental Review. *J. Water Process Eng.* **2020**, *37*, No. 101440.

(17) Yuan, Q.-B.; Guo, M.-T.; Yang, J. Fate of Antibiotic Resistant Bacteria and Genes during Wastewater Chlorination: Implication for Antibiotic Resistance Control. *PLoS One* **2015**, *10*, No. e0119403.

(18) Yan, H.; Lai, C.; Wang, D.; Liu, S.; Li, X.; Zhou, X.; Yi, H.; Li, B.; Zhang, M.; Li, L.; Liu, X.; Qin, L.; Fu, Y. In Situ Chemical Oxidation: Peroxide or Persulfate Coupled with Membrane Technology for Wastewater Treatment. *J. Mater. Chem. A* **2021**, *9*, 11944−11960.

(19) Erasmus, E.; Claassen, J.; Van der Westhuizen, W. Catalytic Wet Peroxide Oxidation of Formic Acid in Wastewater with Naturally-Occurring Iron Ore. *Water SA* **2016**, *42*, 442.

(20) Wang, J.; Chen, H. Catalytic Ozonation for Water and Wastewater Treatment: Recent Advances and Perspective. *Sci. Total Environ.* **2020**, *704*, No. 135249.

(21) Kyzas, G.; Matis, K. Flotation in Water and Wastewater Treatment. *Processes* **2018**, *6*, 116.

(22) Guo, L.; An, Q.-D.; Xiao, Z.-Y.; Zhai, S.-R.; Cui, L. Inherent N-Doped Honeycomb-like Carbon/Fe 3 O 4 Composites with Versatility for Efficient Microwave Absorption and Wastewater Treatment. *ACS Sustainable Chem. Eng.* **2019**, *7*, 9237−9248.

(23) Bray, R. T.; Jankowska, K.; Kulbat, E.; Łuczkiewicz, A.; Sokołowska, A. Ultrafiltration Process in Disinfection and Advanced Treatment of Tertiary Treated Wastewater. *Membranes* **2021**, *11*, 221.

(24) Pino, E.; Calderón, C.; Herrera, F.; Cifuentes, G.; Arteaga, G. Photocatalytic Degradation of Aqueous Rhodamine 6G Using Supported TiO2 Catalysts. A Model for the Removal of Organic Contaminants From Aqueous Samples. *Front. Chem.* **2020**, *8*, 311.

(25) Tauc, J.; Grigorovici, R.; Vancu, A. Optical Properties and Electronic Structure of Amorphous Germanium. *Phys. Status Solidi* **1966**, *15*, 627−637.

(26) D.E.O'C.. Reflectance Spectroscopy (Principles, Methods, Applications). *J. Mol. Struct.* **1972**, *13*, 138.

(27) Regmi, Y. N.; Leonard, B. M. General Synthesis Method for Bimetallic Carbides of Group VIIIA First Row Transition Metals with Molybdenum and Tungsten. *Chem. Mater.* **2014**, *26*, 2609−2616.

(28) Moulder, J.; Stickle, W.; Sobol, P.; Bomben, K. *Handbook of X-Ray Photoelectron Spectroscopy*, In Chastain, J., Ed.; Perkin-Elmer: Eden Prairie: MN, 1992.

(29) Voevodin, A. A.; O'Neill, J. P.; Prasad, S. V.; Zabinski, J. S. Nanocrystalline WC and WC/a-C Composite Coatings Produced from Intersected Plasma Fluxes at Low Deposition Temperatures. *J. Vac. Sci. Technol., A* **1999**, *17*, 986−992.

(30) Czyzniewski, A. Deposition and Some Properties of Nanocrystalline WC and Nanocomposite WC/a-C:H Coatings. *Thin Solid Films* **2003**, *433*, 180−185.

(31) Abad, M. D.; Muñoz-Márquez, M. A.; El Mrabet, S.; Justo, A.; Sánchez-López, J. C. Tailored Synthesis of Nanostructured WC/a-C Coatings by Dual Magnetron Sputtering. *Surf. Coatings Technol.* **2010**, *204*, 3490−3500.

(32) Moulder, J. F.; Stickle, W. F.; Sobol, P. E.; Bomben, K. D. *Handbook of X-Ray Photoelectron Spectroscopy: A Reference Book of Standard Spectra for Identification and Interpretation of XPS Data*; Ulvac-Phi, Inc.: Chigasaki, Japan, 1995; Vol. *80*, pp 40−44.

(33) Lin, H.; Shi, Z.; He, S.; Yu, X.; Wang, S.; Gao, Q.; Tang, Y. Heteronanowires of MoC−Mo 2 C as Efficient Electrocatalysts for Hydrogen Evolution Reaction. *Chem. Sci.* **2016**, *7*, 3399−3405.
(34) Song, H. J.; Sung, M.; Yoon, H.; Ju, B.; Kim, D. Ultrafine A-Phase Molybdenum Carbide Decorated with Platinum Nanoparticles for Efficient Hydrogen Production in Acidic and Alkaline Media. *Adv. Sci.* **2019**, *6*, No. 1802135.
(35) Wang, J.; Wei, H.; Chen, X.; Chen, C.; Chen, X. Facile Preparation of N, P Co-Doped Molybdenum Carbide/Porous Carbon Rough Microspheres for Efficient Electrocatalytic Hydrogen Evolution. *Int. J. Hydrogen Energy* **2020**, *45*, 595−604.
(36) Wan, C.; Regmi, Y. N.; Leonard, B. M. Multiple Phases of Molybdenum Carbide as Electrocatalysts for the Hydrogen Evolution Reaction. *Angew. Chem.* **2014**, *126*, 6525−6528.
(37) Wei, H.; Xi, Q.; Chen, X.; Guo, D.; Ding, F.; Yang, Z.; Wang, S.; Li, J.; Huang, S. Molybdenum Carbide Nanoparticles Coated into the Graphene Wrapping N-Doped Porous Carbon Microspheres for Highly Efficient Electrocatalytic Hydrogen Evolution Both in Acidic and Alkaline Media. *Adv. Sci.* **2018**, *5*, No. 1700733.
(38) Hu, Z.; Zhang, L.; Huang, J.; Feng, Z.; Xiong, Q.; Ye, Z.; Chen, Z.; Li, X.; Yu, Z. Self-Supported Nickel-Doped Molybdenum Carbide Nanoflower Clusters on Carbon Fiber Paper for an Efficient Hydrogen Evolution Reaction. *Nanoscale* **2021**, *13*, 8264−8274.
(39) Xing, J.; Lin, F.; Huang, L.; Si, Y.; Wang, Y.; Jiao, L. Coupled Cobalt-Doped Molybdenum Carbide@N-Doped Carbon Nanosheets/Nanotubes Supported on Nickel Foam as a Binder-Free Electrode for Overall Water Splitting. *Chinese J. Catal.* **2019**, *40*, 1352−1359.
(40) Arrigo, R.; Schuster, M. On the High Structural Heterogeneity of Fe-Impregnated Graphitic-Carbon Catalysts from Fe Nitrate Precursor. *Catalysts* **2019**, *9*, 303.
(41) Mentoor, K.; Twigge, L.; Niemantsverdriet, J. W. H.; Swarts, J. C.; Erasmus, E. Silica Nanopowder Supported Frustrated Lewis Pairs for CO 2 Capture and Conversion to Formic Acid. *Inorg. Chem.* **2021**, *60*, 55−69.
(42) Conradie, M. M.; Conradie, J.; Erasmus, E. Immobilisation of Iron Tris(β-Diketonates) on a Two-Dimensional Flat Amine Functionalised Silicon Wafer: A Catalytic Study of the Formation of Urethane, from Ethanol and a Diisocyanate Derivative. *Polyhedron* **2014**, *79*, 52−59.
(43) van As, A.; Joubert, C. C.; Buitendach, B. E.; Erasmus, E.; Conradie, J.; Cammidge, A. N.; Chambrier, I.; Cook, M. J.; Swarts, J. C. Tetrabenzoporphyrin and -Mono-, - Cis -Di- and Tetrabenzotriazaporphyrin Derivatives: Electrochemical and Spectroscopic Implications of Meso CH Group Replacement with Nitrogen. *Inorg. Chem.* **2015**, *54*, 5329−5341.
(44) Buitendach, B. E.; Erasmus, E.; Landman, M.; Niemantsverdriet, J. W. Hans.; Swarts, J. C. Consequences of Electron-Density Manipulations on the X-Ray Photoelectron Spectroscopic Properties of Ferrocenyl-β-Diketonato Complexes of Manganese(III). Structure of [Mn(FcCOCHCOCH 3) 3]. *Inorg. Chem.* **2016**, *55*, 1992−2000.
(45) Buitendach, B.; Erasmus, E.; Niemantsverdriet, J.; Swarts, J. Properties of Manganese(III) Ferrocenyl-β-Diketonato Complexes Revealed by Charge Transfer and Multiplet Splitting in the Mn 2p and Fe 2p X-Ray Photoelectron Envelopes. *Molecules* **2016**, *21*, 1427.
(46) Erasmus, E. Spectroscopic Monitoring of Carbonylation Reactions on Zeolite Supported Rhodium(I) Carbonyls. *Inorganica Chim. Acta* **2016**, *451*, 197−201.
(47) Erasmus, E. Electronic Effects of Group Fragments on the XPS of Fe 2p and 3p Photoelectron Lines of Ferrocenyl-Containing Chalcones. *South African J. Chem.* **2017**, *70*. DOI: 10.17159/0379-4350/2017/v70a13.
(48) Swart, M. R.; Bezuidenhoudt, B. C. B.; Marais, C.; Erasmus, E. Spectroscopic Characterisation of Grubbs 2nd Generation Catalyst and Its P-Cresol Derivatives. *Inorganica Chim. Acta* **2021**, *514*, No. 120001.
(49) Chauhan, R.; Kumar, A.; Chaudhary, R. P. Photocatalytic Degradation of Methylene Blue with Fe Doped ZnS Nanoparticles. *Spectrochim. Acta, Part A* **2013**, *113*, 250−256.
(50) Supriya, S.; Sathish, S. Enhanced Photocatalytic Decolorization of Congo Red Dye with Surface-Modified Zinc Oxide Using Copper(II)−Amino Acid Complex. *Inorg. Nano-Metal Chem.* **2020**, *50*, 100−109.

https://doi.org/10.1021/acsomega.2c01727
ACS Omega 2022, 7, 23401−23411